Detailed Experimental Information

The MgO used as support was obtained by calcination in air at 450ºC for three hours of a Mg(OH)$_2$ commercial sample from Alfa Aesar. The BET surface area of the obtained MgO was 62 m^{2}g^{-1}. Calcination of the oxide at 950ºC decreased its surface area down to 31 m^{2}g^{-1}.

The Ce$_{0.5}$Tb$_{0.5}$O$_x$ (3% mol.)/MgO catalyst was prepared by incipient wetness impregnation using an acetone solution containing equimolar concentrations of Ce(NO$_3$)$_3$·6H$_2$O and Tb(NO$_3$)$_3$·6H$_2$O. Acetone was used as solvent, instead of water, in order to avoid the uncontrolled dissolution of MgO by acid-base reaction with the impregnating solution. Let us recall at this respect that MgO is a basic oxide and that aqueous solutions of metals are highly acidic. To avoid the fast evaporation of the solvent during the deposition of the lanthanides, the impregnation step was carried out at -10ºC in a single step. The concentration of the solution containing the two lanthanides was adjusted to obtain a final molar loading of 3%.

After impregnation, the catalyst was dried in oven at 105ºC overnight, grounded in an agate mortar, sieved through a 75 μm mesh and further calcined under air in an oven at 500ºC. A 5ºC/min heating ramp was used for the calcination step. Temperature was kept for 1h at 500ºC and then the solid was cooled down under air to room temperature and finally stored in a desiccator. This sample will be referred in the following as Ce$_{0.5}$Tb$_{0.5}$O$_x$ (3% mol.)/MgO.

To study the influence of high temperatures treatments on textural, compositional, structural and functional properties, a portion of the Ce$_{0.5}$Tb$_{0.5}$O$_x$ (3% mol.)/MgO catalyst was submitted to a redox aging cycle consisting of the following steps:

Severe Reduction or SR: heating under a flow of H$_2$(5%)/Ar (60 cm^3·min^{-1}) from room temperature up to 950ºC, at a heating rate of 10 ºC min^{-1} and followed by 2 h of isothermal treatment at 950ºC. Next, the gas flow was switched to He (60 cm^3 min^{-1}), for 1 h, and the sample was cooled down to 25ºC under inert gas flow (60 cm^3·min^{-1}).

After this SR step, the aging cycle was closed by applying a mild re-oxidation, MO, routine. To prevent overheating of the reduced mixed oxides, this part of the cycle started with a very low temperature re-oxidization at -80ºC, by flowing an O$_2$(5%)/He mixture (60 cm^3·min^{-1}) for 1h over the catalyst. The sample was then allowed to freely warm up to room temperature under the same flow of O$_2$(5%)/He (60 cm^3·min^{-1}) and then from room temperature up to 500ºC using a heating ramp of 10ºC/min. After reaching this temperature, the oxidation treatment was prolonged for 1 h. Finally, the sample was cooled down under the same atmosphere to room temperature. In the following this catalyst will be referred as Ce$_{0.5}$Tb$_{0.5}$O$_x$ (3% mol.)/MgO SRMO.

A TbO$_x$ (3% mol.)/MgO was also prepared as reference using the same synthesis route.

Textural properties of the samples were determined by N$_2$ adsorption at -196 ºC using a Quantachrome Autosorb iQ automatic device. Before measurement, samples were pre-evacuated at 200ºC for 2 h.

Inductively coupled plasma-atomic emission spectrometry (ICP-AES) was employed to determine the Ce and Tb loadings of the catalyst. X-ray diffraction (XRD) analyses of the catalysts were carried out using a Bruker diffractometer Model D8 ADVANCE operated at 40 kV and 40 mA employing Cu Kα radiation.

Temperature Programmed Reduction experiments under hydrogen, H$_2$-TPR-MS, were performed in an experimental device coupled to a Pfeiffer, model Thermostar QME-200-D-35614, quadrupole mass spectrometer using 200 mg of sample, a 5% H$_2$/Ar flow rate of 60 cm^3 min^{-1} and a heating ramp of 10 ºC min^{-1}. Prior to all the H$_2$-TPR runs, the samples were cleaned by heating up to 500ºC under 5% O$_2$/He flowing at 60 cm^3 min^{-1}, at a heating rate of 10 ºC min^{-1}; then, they were kept for 1 h at this temperature and further cooled down to 150ºC under the flow of diluted oxygen and finally to 25ºC in He. The results are presented in the form of water evolution (mass/charge ratio=18) *vs* temperature, during the reduction process.

For a quantitative analysis of the reduction process, H$_2$-TPR was also performed using the Thermal Conductivity Detector (TCD) of an Autochem Micromeritics apparatus. The amount of sample routinely used in these experiments was 30 mg, the 5% H$_2$/Ar flow rate was 25 cm^3 min^{-1}, and the heating ramp was 10°C min^{-1}. Prior to all the TPR runs the samples were cleaned by heating them under flowing He at 25 cm^3 min^{-1}, at a heating rate of 10°C min^{-1}, up to 500°C. Then, they were kept for 1h at this temperature and cooled down to 150ºC under the flow of diluted oxygen and finally to 25ºC in He.

Ultimate Oxygen Storage Capacity (OSC) values were obtained from oxygen volumetric chemisorption experiments. The isotherms were recorded at 200ºC on a Micromeritics ASAP 2020 instrument in the oxygen

partial pressure interval 0–300 Torr. The samples (400 mg) were pre-reduced by heating in a flow of 5% H_2/Ar (60 cm^3 min^{-1}) at 10 ºC min^{-1}, from 25ºC up to the selected reduction temperature (T_{redn}); they were kept at T_{redn} for 1 h under flowing 5% H_2/Ar; then they were evacuated for 1 h (residual pressure < 1.10^{-6} Torr) at T_{redn} or 500ºC if T_{redn} was lower than 500ºC) and then finally cooled down to 200ºC under high vacuum. These evacuation conditions ensure the elimination of any significant amount of hydrogen chemisorbed on the oxides.

Samples for TEM/STEM analysis were obtained by directly depositing a tiny portion of the nanocrystal powders onto holey carbon-coated TEM grids at room temperature in order to avoid contact with any solvent which could cause contamination during STEM observation. TEM/STEM characterization was performed using a FEI Titan Cubed Themis 60-300 microscope, equipped with a monochromator, operated at 200 kV and 80 kV. For HR-STEM-HAADF imaging, a semi convergence angle of 20 mrad was used together with a camera length of 115 mm. This microscope was equipped with a high efficiency XEDS ChemiSTEM system implementing 4 windowless SDD detectors [L. J. Allen, A. J. D'Alfonso, B. Freitag and D. O. Klenov, *MRS Bull.*, 2012, **37**, 47–52]. Quantification of the XEDS data was performed using the Bruker ESPRIT software. Very high spatial resolution EELS experiments were performed working in the spectrum imaging (SI) mode [C. Jeanguillaume and C. Colliex, Ultramicroscopy, 1989, 28, 252–257], which allows the correlation of analytical and structural information of selected regions of the material under study. In this technique, the EELS and HAADF signals are collected simultaneously while the electron beam is scanned across the selected area of the sample. The SI experiments were acquired in Dual EELS mode using an energy dispersion of 0.25 eV, 80 pA probe current and 100 ms acquisition time per EELS spectrum. In the Dual EELS mode, the zero-loss region is recorded simultaneously with the core-loss signal of the element(s) of interest, which allows a very precise determination of the absolute value of the energies at which the core-loss edges are appearing in the experiment. The latter is a key aspect when the determination of oxidation states of the elements is pursued in the EELS experiment. In our case, Ce and Tb $M_{4,5}$ (885-905 eV, 1241-1275 eV, respectively) elemental and oxidation state maps were built after removing the background from raw data, using a power law model and a window width of 25 eV. HREM images were recorded at 80 kV by exciting the monochromator up to 0.4, which allowed obtaining an energy resolution of 200meV. Afterwards, the aberration of the objective lens was corrected up to fourth-order using the Zemlin tableau.

X-ray Photoelectron Spectra were obtained using a Kratos Axis Ultra DLD instrument, and recorded with monochromatic Al Kα radiation (1486.6 eV). The instrument was operated in the fixed analysis transmission mode (FAT), using pass energy of 20 eV. The Kratos coaxial charge neutralization system was used to compensate charging effects, and the binding energy scale was calibrated with respect to binding energy (BE) scale was calibrated with respect to the highest BE peak for Ce 3d core level (u''') at 917.0 eV. [J. P. Holgado, R. Alvarez and G. Munuera, Appl. Surf. Sci., 2000, 161, 301–315]. CasaXPS software (version 2.3.19rev1.1m), Casa Software Ltd., Devon, UK, 2017) was used for spectra processing.

The methane combustion experiments were performed in an experimental device coupled to a Pfeiffer, model Thermostar QME-200-D35614, quadrupole mass spectrometer using 150 mg of sample. The reaction gases for methane combustion consisted of a mixture of 2.5% CH_4 and 6.0% O_2 in He. The flow rate of the feed gas was 80 cm^3 min^{-1} and a heating ramp of 10 ºC min^{-1} was used. Prior to all the experiments, the samples were cleaned by heating up to 500ºC under 5% O_2/He flowing at 60 cm^3 min^{-1}, at a heating rate of 10 ºC min^{-1}. Then, they were kept for 1 h at this temperature and further cooled down to 150ºC under the flow of diluted oxygen and finally to 25ºC under He. The activity results are presented in the form of total percent of methane vs reaction temperature.
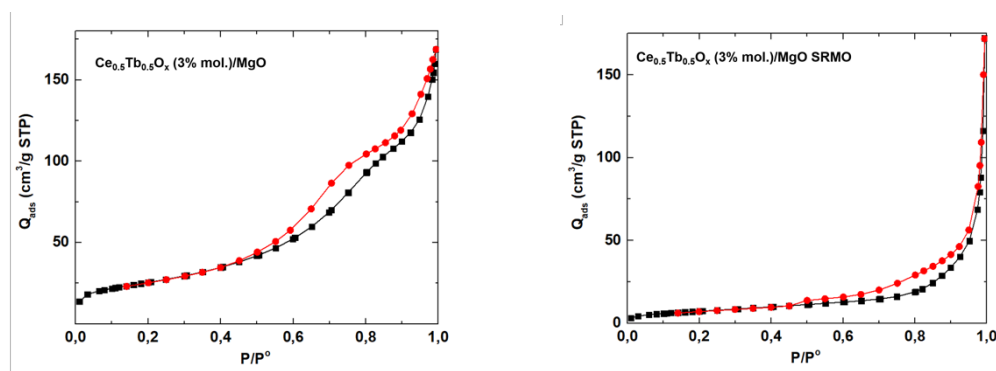

Figure S1. Adsorption/Desorption branches of the N_2 isotherms recorded on $Ce_{0.5}Tb_{0.5}O_x$(3% mol.)/MgO and $Ce_{0.5}Tb_{0.5}O_x$(3% mol.)/MgO SRMO.
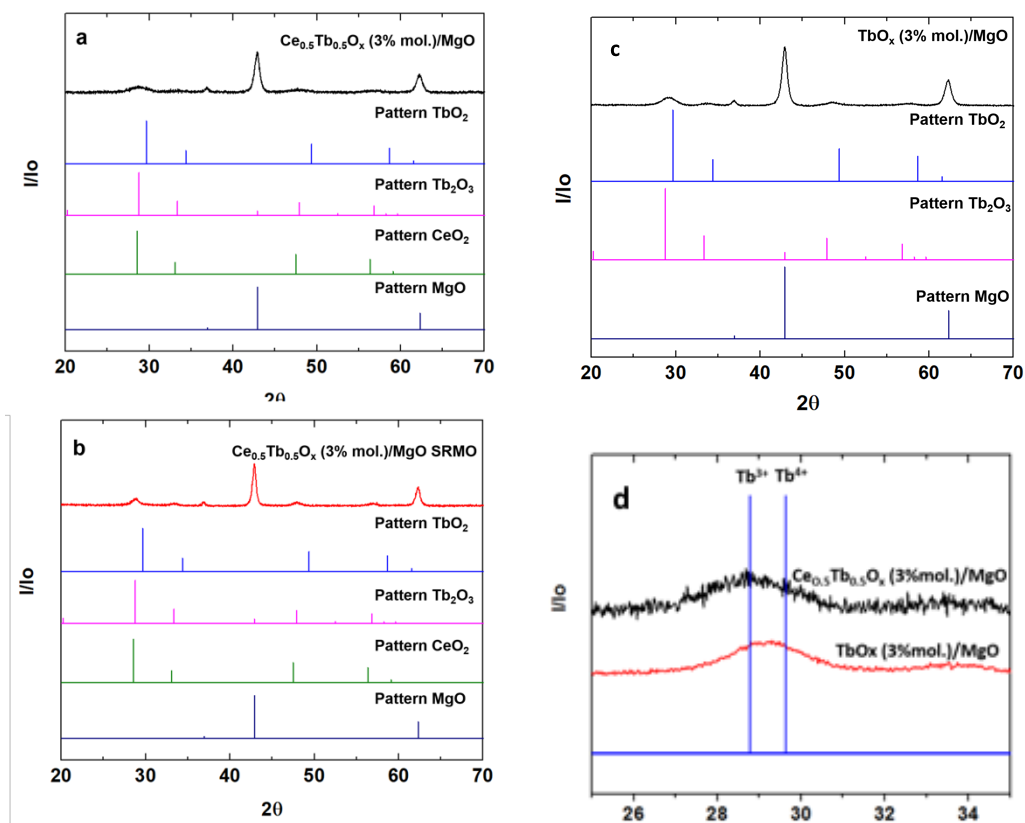
Figure S2. X-Ray Diffraction (XRD) (a) Ce$_{0.5}$Tb$_{0.5}$O$_x$(3% mol.)/MgO (b) Ce$_{0.5}$Tb$_{0.5}$O$_x$(3% mol.)/MgO SRMO; (c) TbOx (3% mol.)/MgO; (d) Enlargement of the 25-35 2Θ region ({111} fluorite peak) of the two Tb-containing catalysts. Line diagrams depicting the position of reflections of reference phases are included for comparison.
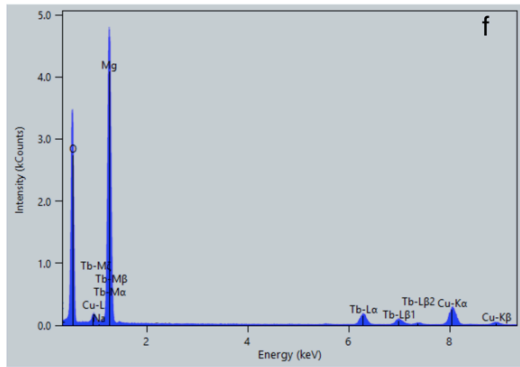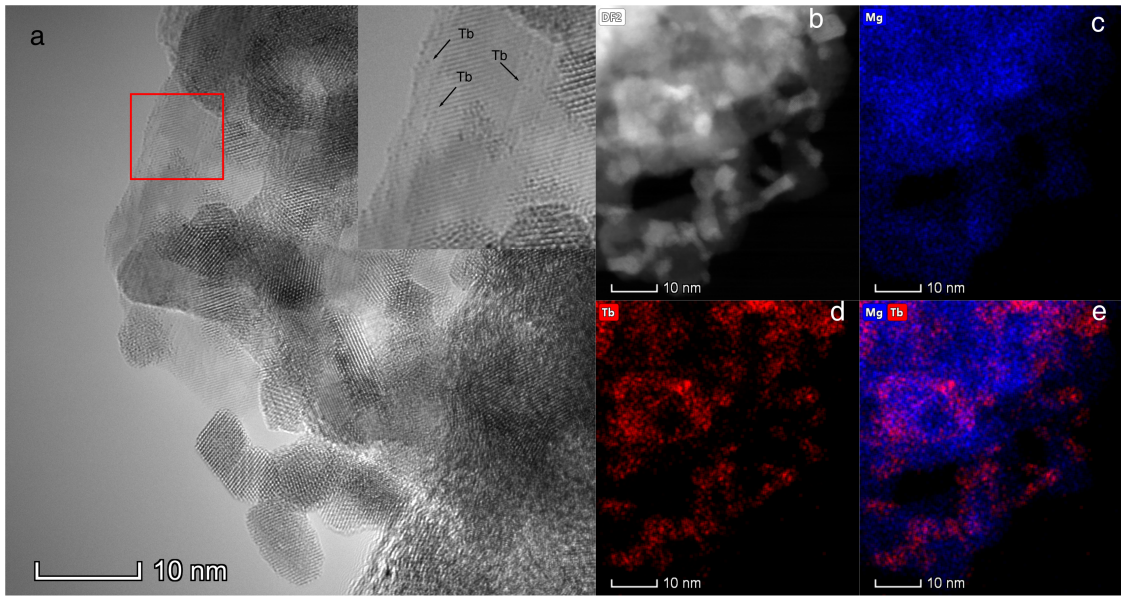
Figure S3.-Results of the TEM/STEM study of the TbOx (3% mol.)/MgO catalyst: (a) AC-HRTEM images; (b) STEM-HAADF image; (c-e) Mg, Tb and composite elemental maps; (f) EDS spectra of the whole area.
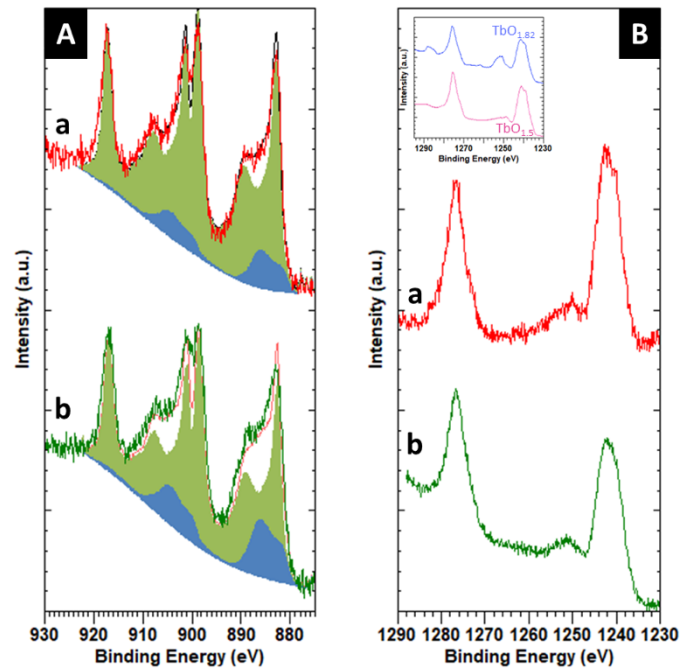
Figure S4. Ce3d (A) and Tb3d (B) XPS signals of $Ce_{0.5}Tb_{0.5}O_x$(3% mol.)/MgO (a) and $Ce_{0.5}Tb_{0.5}O_x$(3% mol.)/MgO SRMO (b). Ce 3d peak decomposition using reference Ce^{4+} (green) and Ce^{3+} (blue) spectra. Inset in (B) shows reference spectra for $TbO_{1.82}$ (mixed Tb^{4+} and Tb^{3+}) and $TbO_{1.5}$ (pure Tb^{3+}).
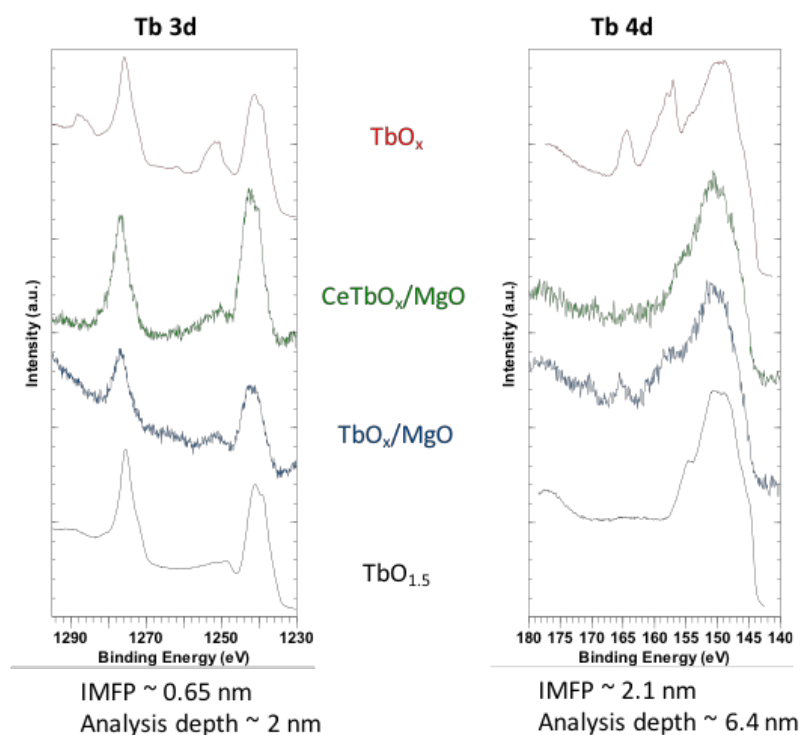
Figure S5.- Comparison of the Tb 3d and 4d XPS spectra in the TbO_x (3%mol.)/MgO and $Ce_{0.5}Tb_{0.5}O_x$(3% mol.)/MgO catalysts.

Table S1. XPS quantification of the prepared catalysts.

SAMPLE	Ce 4d/Tb 4d	(Ce 4d+Tb 4d) / Mg 2s	(Ce 3d+Tb 3d) / Mg 1s	C 1s (carbonate) / Mg 1s
$Ce_{0.5}Tb_{0.5}O_x$(3% mol.)/MgO	1.1±0.1	0.42	0.84	0.37
$Ce_{0.5}Tb_{0.5}O_x$(3% mol.)/MgO SRMO	1.3±0.1	0.22	0.35	0.14
TbOx (3% mol.)/MgO	-	0,07	0,07	-

(1) The Ce/Tb molar ratio, 1.1, as determined from the integrated intensities of the Ce 4d and Tb 4d signals, is exactly that expected from the ICP determined values (1.6 / 1.5 = 1.1).

(2) The value of the (Ce 4d + Tb 4d)/Mg 2s intensity ratio, 0.27, is much higher than than corresponding to the bulk value, 0.031 (=3/97), which clearly evidences that the two lanthanides concentrate on the surface. To understand this question, it is important to take into account that the values of the inelastic mean free path (IMFP) of Ce 4d, Tb 4d and Mg 2s photoelectrons are 2.18 nm, 2.13 nm and 2.21 nm and also that about 95% of the XPS signal comes from roughly 3 times the IMPF, i.e. ≈ 6 nm. The same is observed when the (Ce 3d + Tb 3d)/Mg 1s ratio, 0.67, is compared with the average composition of the catalyst. Since the depth of analysis in the later case is smaller, roughly less than 3 nm, the much larger deviation between the XPS and average ratios clearly points out to a concentration of the lanthanides in the very first atomic layers of the surface.

(3) The total lanthanide 4d/Mg2s and total lanthanide/Mg1s ratios are much smaller in the TbOx (3% mol.)/MgO catalyst, which evidences a much lower dispersion of the supported phase in this catalyst.
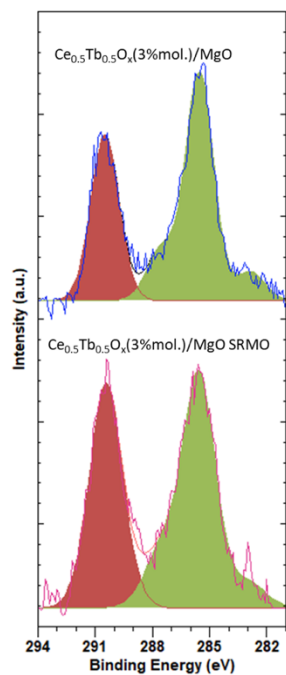
Figure S6. C1s XPS signals corresponding to $Ce_{0.5}Tb_{0.5}O_x$(3% mol.)/MgO and $Ce_{0.5}Tb_{0.5}O_x$(3% mol.)/MgO SRMO. Signals corresponding to carbonate surface species are represented in red.
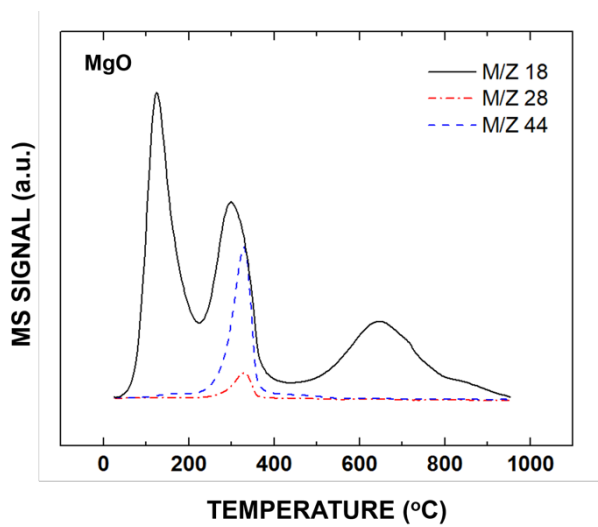

Figure S7. O_2-TPO-MS analysis of the MgO support

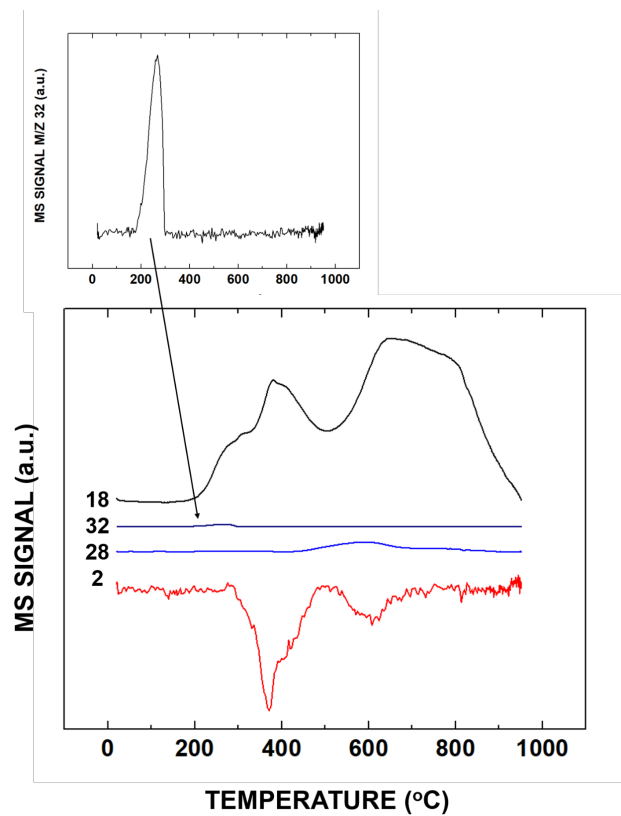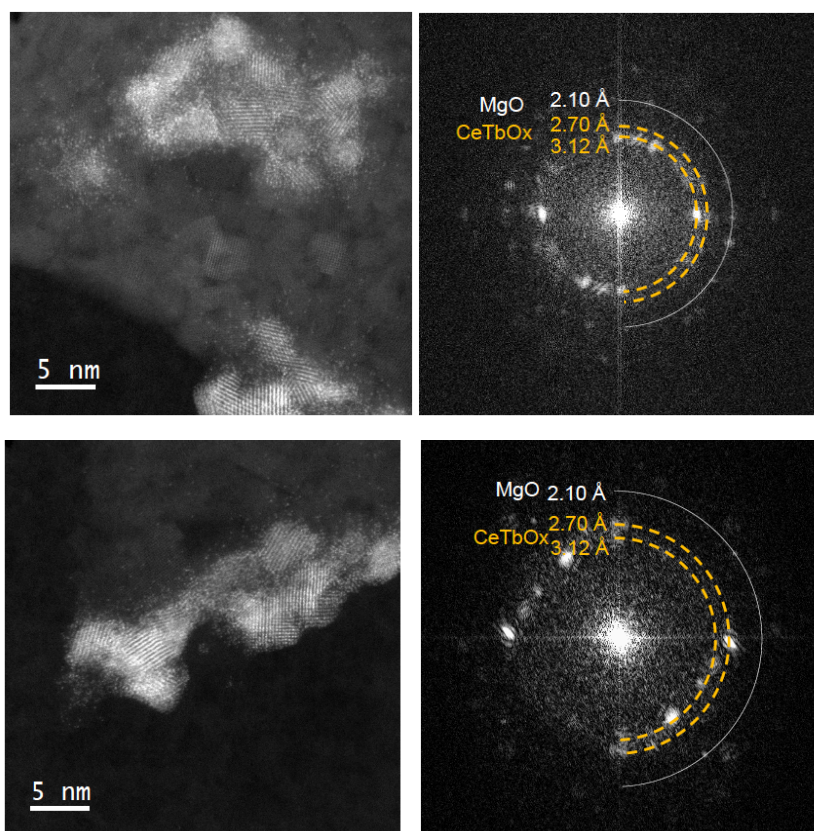Figure S8. H$_2$-TPR-MS of the reference TbO$_x$(3% mol.)/MgO catalyst.

Figure S9. (left column) HR-STEM-HAADF images of the Ce$_{0.5}$Tb$_{0.5}$O$_x$ (3% mol.)/MgO catalyst; (right column) Diffractograms of the whole areas depicting rings of diffraction spots corresponding to both MgO and fluorite phases.

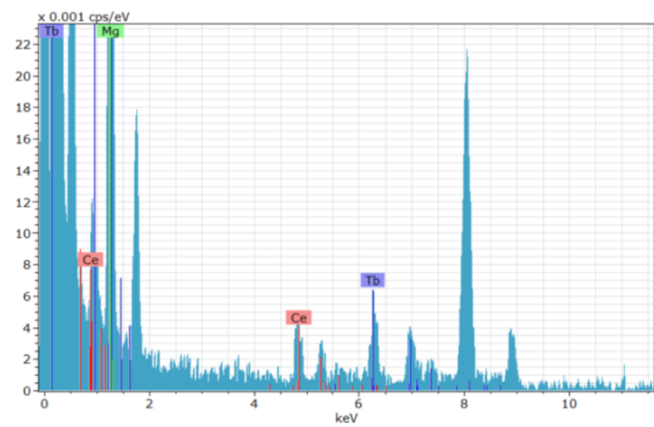Figure S10. Illustrative EDS spectrum of a large area in the fresh $Ce_{0.5}Tb_{0.5}O_x$ (3% mol.)/MgO catalyst. Both Ce and Tb peaks are detected. Quantification indicates Ce and Tb molar contents of 42% and 58%, respectively.
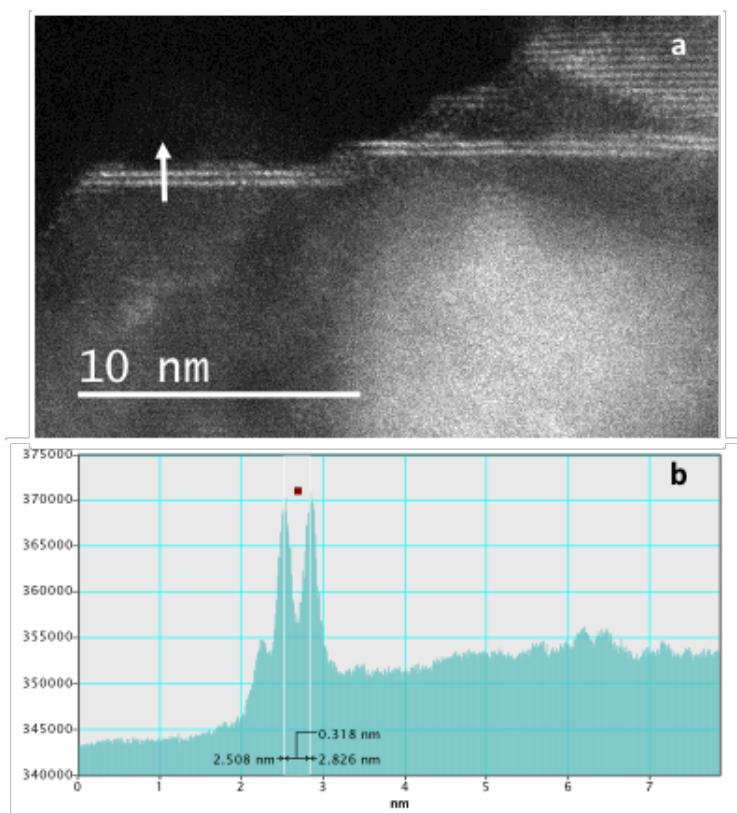

Figure S11. (a) HR HAADF-STEM image of a fluorite bilayer. The position where the intensity profile shown in (b) was recorded is marked by a white arrow. The 0.318 nm distance is very close to that of bulk {111} CeO_2 (0.312 nm).
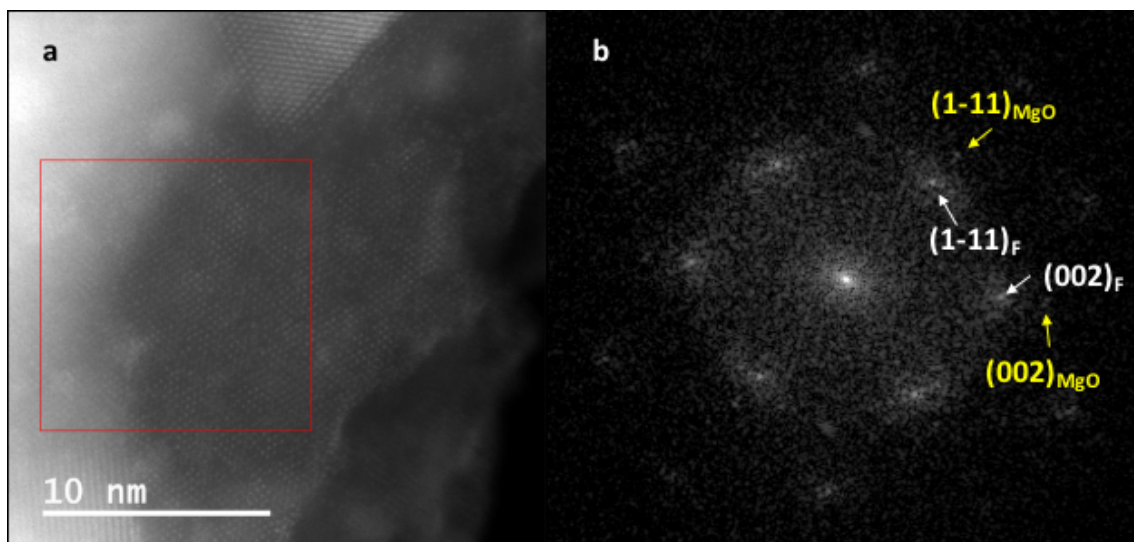
Figure S12. (a) HR HAADF-STEM image shown a fluorite bilayer in top view. The digital diffractogram shown in (b) was taken from the area marked in red. The positions of {111} and {002} reflections from both the bilayer and the underlying MgO support have been arrowed.
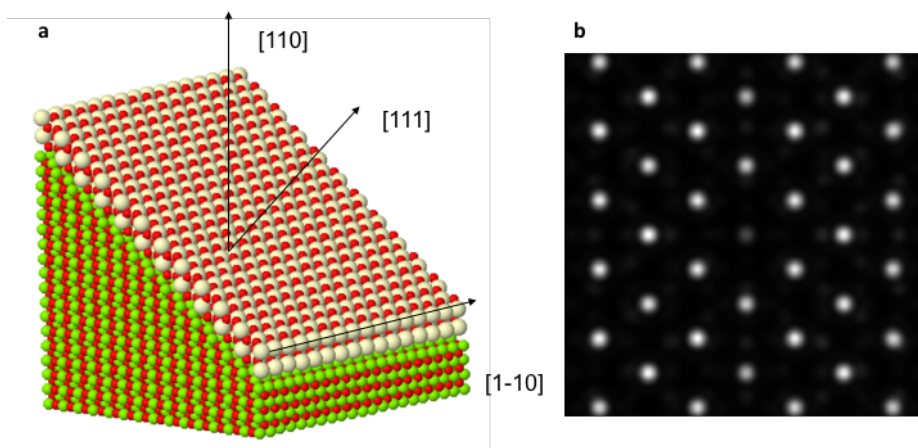

Figure S13 (a) Structural model of a fluorite bilayer grown under parallel orientation relationship on top of a {111} MgO surface; (b) Simalted HR HAADF-STEM image along the [110] zone axis of the two components. Note how the lanthanide atomic columns appear very bright whereas those corresponding to Mg are hardly visible.
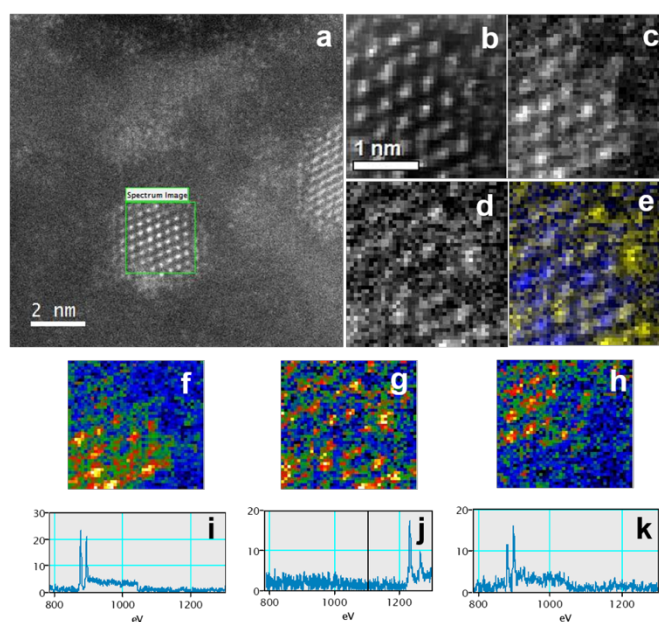

Figure S14. STEM-EELS-SI analysis of the oxidation state of the lanthanides in the bilayers observed in the Ce0.5Tb0.5Ox (3% mol.)/MgO SRMO sample

For the analysis of oxidation states in the bilayers and patches, the collections of EEL spectra were first denoised by the Principal Component Analysis (PCA) method. ADF and chemical maps of Ce and Tb of the structure marked on Figure S14(a), are shown in Figures S14(b)-S14(d). Figure S14(e) corresponds to the composite Ce+Tb signal. Once more, the patch-like distribution of Ce and Tb within the layer is observed. Moreover, taking into account that the fine structure of the $M_{4,5}$ signals of Ce allows differentiating between its +4 and +3 oxidation state, the collections of spectra were analysed by the Non-negative Matrix Factorization Components (NMF) method to map the distribution of the oxidation states of this element at atomic level, Figures S14(f)-(k). The spectra of the bilayers contain three major components; two related to Ce (Ce^{3+}, Figures S14(f) and (i); and Ce^{4+} species, Figures S14(h) and S14(k)), and only one Tb component (Figures S14(g) and S14(j)) which indicates a dominant contribution of Tb^{3+}.
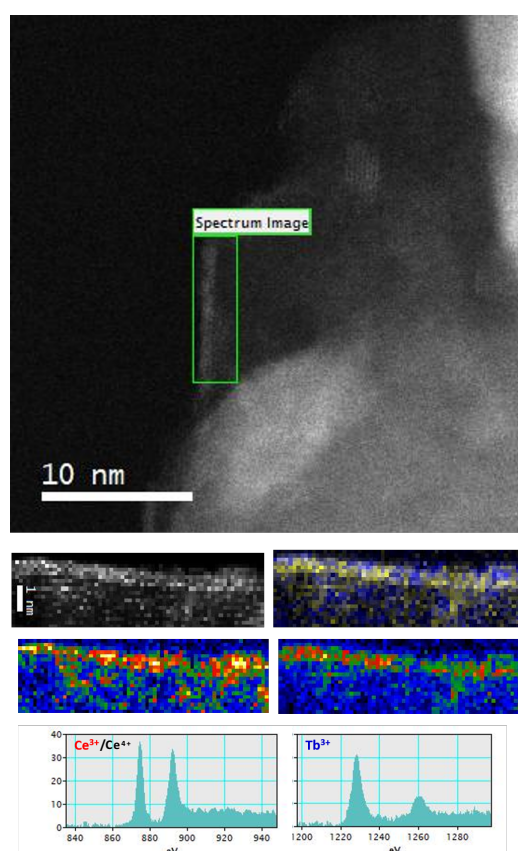

Figure S15. STEM-EELS-SI experiments performed on bilayers imaged in the direction parallel to the interface with the MgO support
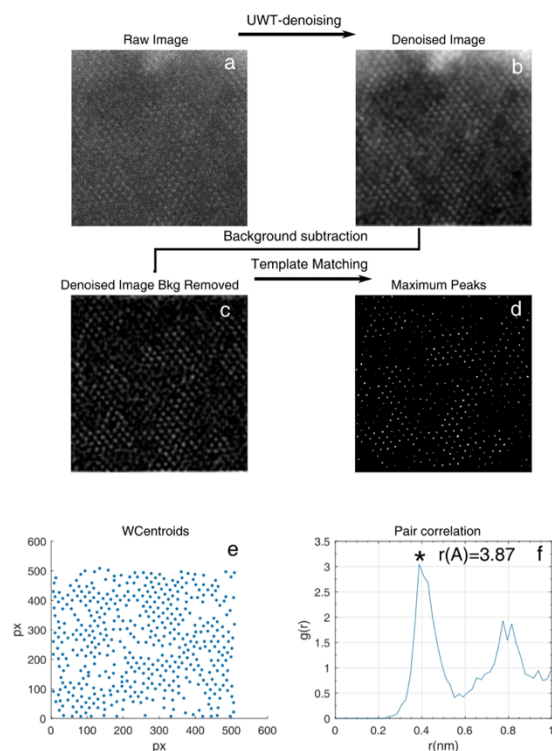
Figure S16. RDF analysis of the HAADF-STEM images of bilayers in $Ce_{0.5}Tb_{0.5}O_x$ (3% mol.)/MgO SRMO.

Figures S16(a) and (b) depict the contrasts of a HAADF-STEM image of a layer, recorded in top view along the [110] direction of the fluorite structure, before and after Undecimated Wavelet Transforms (UWT) denoising. After background subtraction, Figure S16(c), the position of the contrast maxima was automatically determined using the correlation with a template obtained by averaging the contrasts of different atomic column-like contrasts all over the image, Figure S15(d). After this operation, a map of the X-Y position of the centroids of all the detected atomic columns in the image was automatically generated, Figure S16(e).

At the level of first neighbors, the distribution of atomic columns corresponds to that expected for a perfect structure, but there are evident distortions at larger distances as well as differences in the occupation of atomic columns, in such a way that certain columns appear as missing.

The local disorder at medium distances may explain why in the HAADF-STEM images of the bilayers recorded edge-on view, as that in Figure 5(a), the fluorite structure of the mixed ceria-terbia oxide is not clearly revealed.

The structural models obtained after template matching allows also determining Radial Distribution Function (RDF) of the atomic columns, Figure S16(f). Note that the RDF shows a first maximum at 0.387 nm overlapped with a second around 0.420 nm. These distances are larger than those expected for the Ce-Ce or Tb-Tb distances in the [110] projection of a fluorite structure (0.331 nm and 0.382 nm). This indicates that the growth of the (111) bilayers on top of the (111) MgO planes involves some strain.
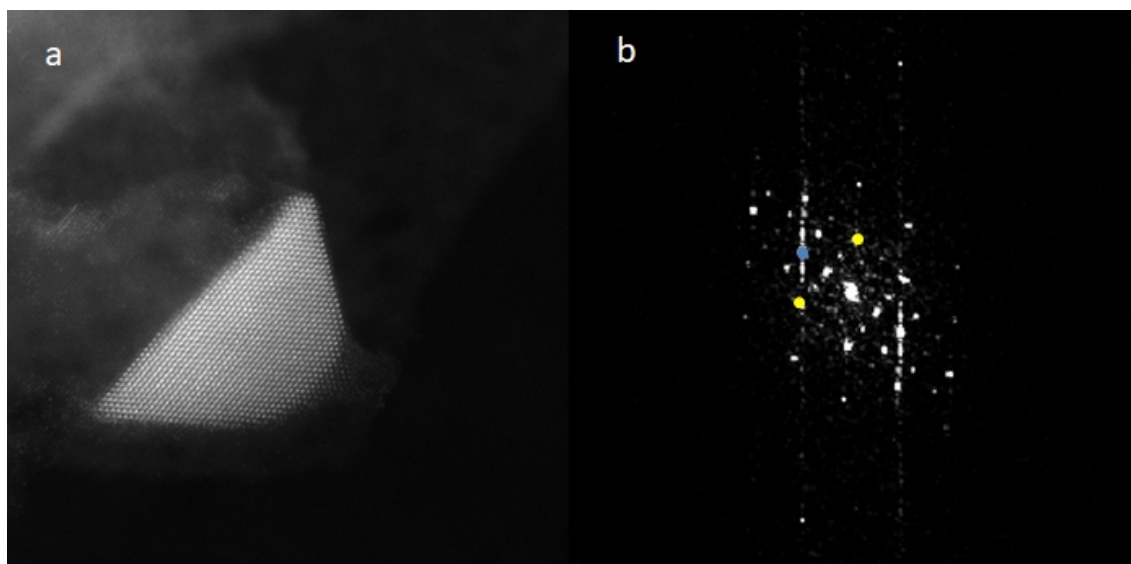
Figure S17. (a) HAADF-STEM image of a 3D nanoparticle in the $Ce_{0.5}Tb_{0.5}O_x$ (3% mol.)/MgO SRMO catalyst. The diffractogram from this particle in (b) show fluorite superstructure features. The reflections colored in yellow and light blue correspond to the basic {111} and {002} reflections of the fluorite. Note the presence of ½ {200} reflections as well as a set of 3 extra reflections in between the {111}s, i.e. along the <220>* reciprocal direction.

Note how in the diffractogram of the image in Figure S17(b), the (200) spot of $Ce_{0.5}Tb_{0.5}O_x$ is parallel to the (111) of the support.

A quite interesting feature of the structure of the nanoparticles is the alternation of intensities of the {002} type lattice planes, which is particularly well observed at locations as that marked with a rectangle. This image feature is evidenced in the diffractogram of Figure S17(b).

Since the contrasts in STEM-HAADF are dominated by the contribution of the cations, this contrast feature points out to the alternation in space of higher and lower average atomic number planes. Therefore, this observation would suggest the occurrence of alternated Tb-rich and Ce-rich {002} planes. Superstructure features were also observed in the corresponding AC-HRTEM images, Figure S18. However, a detailed analysis by image simulation, Figure S19, indicates that this contrast feature is actually related to the partial reduction of the mixed oxide nanoparticles, which adopt the bixbyite type structure characteristic of the reduced lanthanide oxides with composition in the σ-phase region (C-$LnO_{1.5+x}$). [48] In fact, the reduction degree detected by XPS points at the formation of a phase close to the cubic sesquioxide.

In any case, a small Tb^{4+} content cannot be fully disregarded, which could contribute to the 47% of OSC observed in $Ce_{0.5}Tb_{0.5}O_x$ (3% mol.)/MgO SRMO after reduction at 700ºC; a value higher than that expected from the Tb^{3+} and Ce^{3+} contents detected by XPS.

Whatever the exact reduced phase could be, it seems clear that the superstructure features detected both in HAADF-STEM and HREM images can be fully explained without involving disorder-order transitions in the cationic sublattice, as it has been described for ceria-zirconia mixed oxides submitted to SRMO type treatments. (S. Trasobares, M. López-Haro, M. Kociak, K. March, F. de La Peña, J. A. Perez-Omil, J. J. Calvino, N. R. Lugg, A. J. D'Alfonso, L. J. Allen and C. Colliex, *Angew. Chemie Int. Ed.*, 2011, **50**, 868–872)
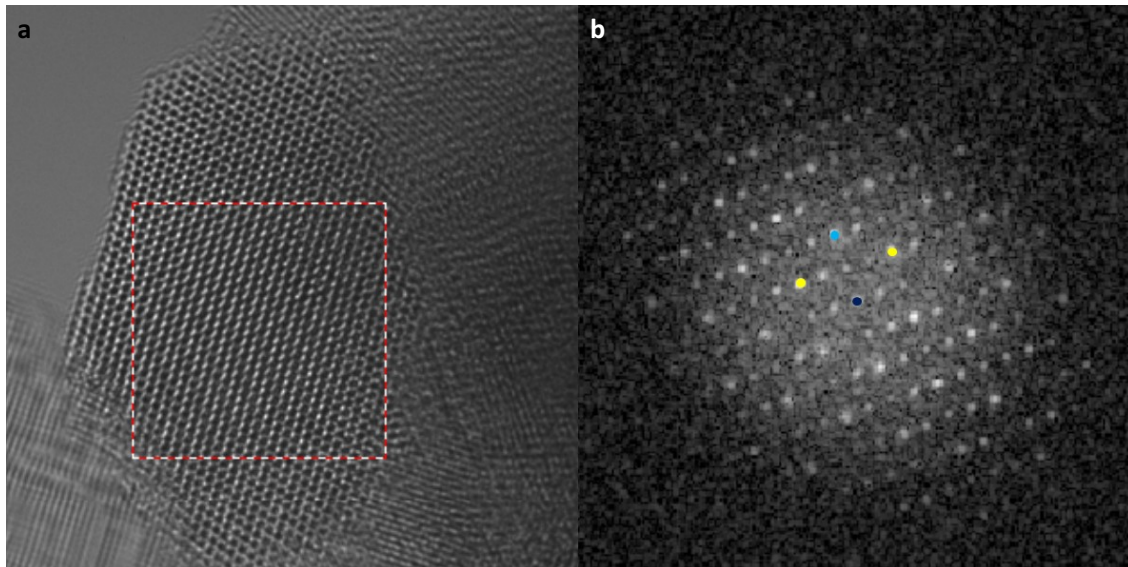
Figure S18. (a) HREM image of a 3D nanoparticles observed in the $Ce_{0.5}Tb_{0.5}O_x$ (3% mol.)/MgO SRMO catalyst. Low frequency contrast modulations are clearly observed both in the image and in the digital diffractogram shown in (b). The center of the diffractogram has been marked in deep blue; the {111} reflections in yellow and the {002} reflection in light blue. Note that there are 3 superstructure reflections between the {111}s (i.e. along te $<220>^*$ reciprocal direction) and only 1 along the $<002>^*$ reciprocal direction. Apart from reflection intensities, this distribution of superstructure spots matches those of both the σ-$LnO_{1.75+x}$ and π-$Ln_{16}O_{30}$ phases.

HREM images of the 3D nanoparticles clearly show the presence of a fluorite superstructure. These superstructure features are observed in the images in the form of low frequency contrast modulations, Figure S18(a), which also reflect in the diffractograms of the HREM images as a set of extra spots located in between those of the fluorite, Figure S18(b). A comparison of the diffractograms in Figures S17(b) and S18(b) with those calculated for the different members of the homologous series of the higher rare earth oxides (C. López-Cartes, J. . Pérez-Omil, J. . Pintado, J. . Calvino, Z. Kang and L. Eyring, Ultramicroscopy, 1999, 80, 19–39) along the [110] zone axis, reveals a good match with both the C-$LnO_{1.5+x}$ and the π-$Ln_{16}O_{30}$ phases ($LnO_{1.875}$).

The reduction degree in the π-$Ln_{16}O_{30}$ phase would involve only 24% reduction of the lanthanides and, therefore, nearly half of the Tb in the nanoparticles to be Tb^{4+}. From XPS the presence of a small fraction of Tb^{4+} in these nanoparticles cannot be fully disregarded since their size, 15-20 nm, is larger than the depth of analysis of the Tb 3d signal. Nevertheless, since EELS results point out to a dominance of Tb^{3+}, the bixbyite type structure seems to be the most likely. In any case, a small Tb^{4+} content cannot be fully disregarded, and in fact it could contribute to the 47% of OSC observed in $Ce_{0.5}Tb_{0.5}O_x$ (3% mol.)/MgO SRMO after reduction at 700ºC; a value higher than that expected from the Tb^{3+} and Ce^{3+} contents detected by XPS, nearly 100% and 23% respectively.
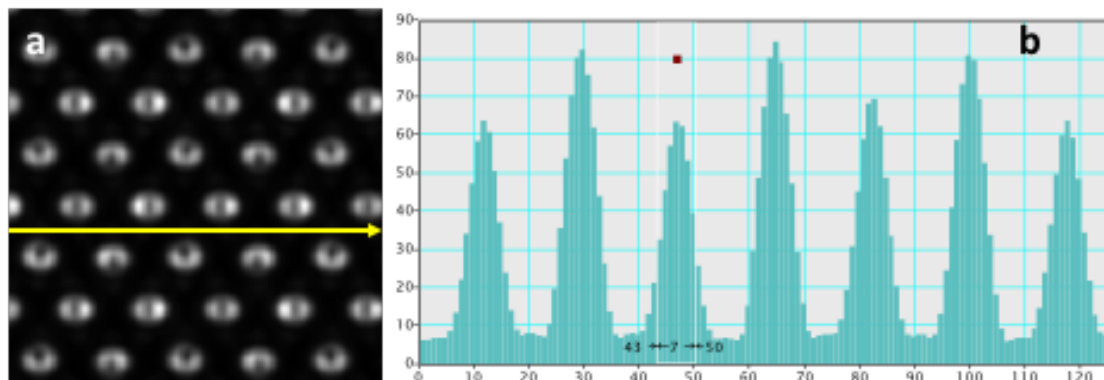

Figure S19. (a) Simulated HR HAADF-STEM image of a C-Ln_2O_3 crystallite along the [110] zone axis; (b) Integrated intensity profile along the [002] direction (as marked with a yellow arrow). Note the alternation in brighter and darker lines. This would result in the contrast pattern observed in the experimental HAADF images of the 3D nanoparticles observed in the $Ce_{0.5}Tb_{0.5}O_x$ (3% mol.)/MgO SRMO catalyst.

A.C. Johnston-Peck et al. (A. C. Johnston-Peck, W.-C. D. Yang, J. P. Winterstein, R. Sharma and A. A. Herzing, Micron, 2018, 115, 54–63) have proved that HR STEM-HAADF images of cubic, fully reduced, ceria, i.e. Ce_2O_3, show double periodicity {002} fringes in images recorded along the [100] zone axis. This is related to the occurrence of subtle displacements in the position of the Ce atom columns linked to structural relaxation around oxygen vacancies. To check if this was also the case in images recorded along the [110] zone axis, a model of the cubic sesquioxide, C-Ln_2O_3, in which the two lanthanides were disordered, was built and the corresponding image calculated, Figure S19(a). It is clear that also along this zone axis a double {200} periodicity is observed, due to the slight shifts of the cation columns with respect to those in the ideal fluorite.
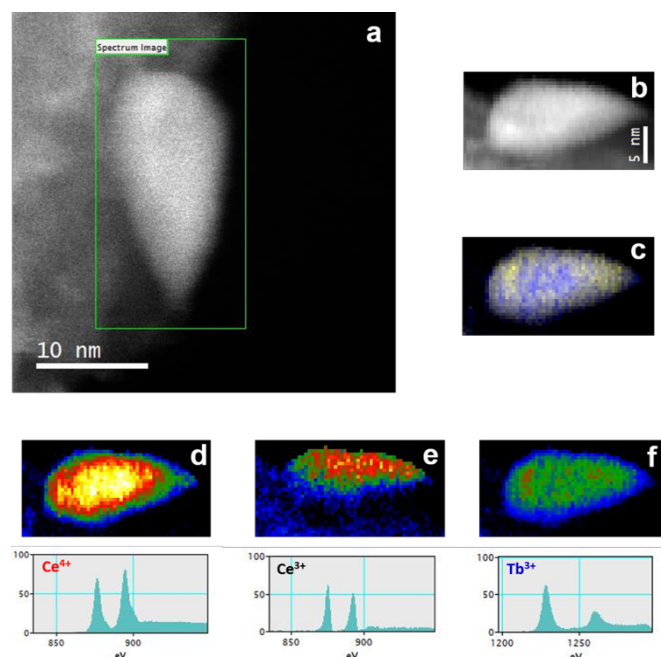

Figure S20. STEM-EELS-SI image recorded on the 3D nanoparticles of medium size 10-20 nm in $Ce_{0.5}Tb_{0.5}O_x$(3% mol.)/MgO-SRMO.

The spatial distribution and the oxidation states of Ce in these 3D nanoparticles were also investigated by means of STEM-EELS-SI, Figures S20 and S21. Figure S20(a) shows a HAADF-STEM image where one of these studies was performed. Figure S20(b) depicts the ADF image of the area where the SI signal was acquired. The analysis of the whole collection of spectra by PCA and NMF reveals the presence of three independent components, one due to Ce^{3+}, another due to Ce^{4+} and a third one related to Tb. The maps of these three components are shown as Figures S20(d) through S20(f). The intensity of the component in each pixel is color-coded, in such a way that blue represents the lowest intensity and yellow the highest one. Note, first, that both (Ce^{3+} + Ce^{4+}) and Tb signals are present throughout the nanoparticle volume, from surface to bulk, which indicates mixture of the two components at the atomic level.

Concerning the oxidation states of Ce, it is clear that both Ce^{3+} and Ce^{4+} are present in the bulk and in the surface. The intensity distribution of Ce^{3+} looks more homogeneous, whereas the signal of Ce^{4+} gets more intense at the thicker parts of the nanoparticle. Moreover, the area covered by the Ce^{3+} signal is slightly smaller than that of Ce^{4+}, the intensity of the former being lost at locations close to the interface with the MgO support. These observations suggest the likely presence of a Ce^{3+} shell covering the particle and an accumulation of oxidized Ce at the interfaces with the MgO support. Additional STEM-EELS-SI results included in Figure S21 provide further support to these evidences.
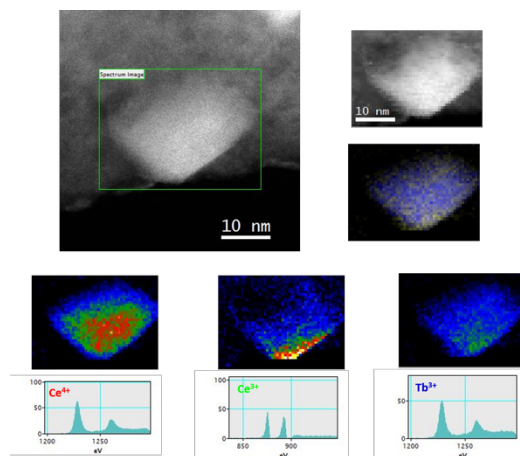
Figure S21. Figure 11. STEM-EELS-SI image recorded of 3D nanoparticles of medium size, 10-20 nm in $Ce_{0.5}Tb_{0.5}O_x$(3% mol.)/MgO-SRMO sample.